

# A Numerical Investigation of Analyte Size Effects in Nanopore Sensing Systems

Kai Szuttor,<sup>1</sup> Patrick Kreissl,<sup>1</sup> and Christian Holm<sup>1</sup>

*Institute for Computational Physics, Universität Stuttgart, Allmandring 3, D-70569 Stuttgart, Germany*

(\*holm@icp.uni-stuttgart.de)

(\*kai@icp.uni-stuttgart.de)

(Dated: 2 August 2021)

We investigate the ionic current modulation in DNA nanopore translocation setups by numerically solving the electrokinetic mean-field equations for an idealized model. Specifically, we study the dependence of the ionic current on the relative length of the translocating molecule. Our simulations show a significantly smaller ionic current for DNA molecules that are shorter than the pore at low salt concentrations. These effects can be ascribed to the polarization of the ion cloud along the DNA that leads to an opposing electric dipole field. Our results for DNA shine light on the observed discrepancy between infinite pore models and experimental data on various sized DNA complexes.

## I. INTRODUCTION

The basis of molecule sensing using nanopores is the modulation of the ionic current in a setup where two electrolyte reservoirs are connected by a nanopore. An externally applied electric field causes an ionic current and drives a charged particle or molecule through the nanopore. During the translocation a salt-dependent ionic current modulation can be observed. Such systems have been employed for a range of analytes from DNA and proteins to viruses<sup>1-3</sup>. A recent study<sup>4</sup> even combined the nanopore sensing with machine learning to differentiate different coronaviruses based on their footprint in the current signal. Nanopore sensing has been thoroughly investigated to study the current modulation caused by DNA molecules, both experimentally<sup>5-16</sup> and via numerical simulations<sup>17-30</sup> using a multitude of simulation approaches<sup>31</sup>. A general overview of hydrodynamic and transport phenomena in solid-state nanopores is given in several review articles<sup>32-34</sup>. In theory such systems have often been investigated with so-called infinite pore models<sup>22,27,28,35</sup>. These models neglect any finite-length effects of the DNA molecule or the pore by inherently assuming a translational symmetry. For the translocation of a single double-stranded DNA (dsDNA) molecule through a cylindrical pore it has been shown<sup>28</sup> that infinite pore models agree very well with the experimental data<sup>9,13</sup> for the current modulation. While in these dsDNA nanopore systems the assumption of an infinitely short pore holds, we want to explore the opposite limit in which the analyte size approaches the length of the pore or is even shorter than the pore. Therefore, we cover analyte-to-pore length ratios smaller than unity. This range might, *e. g.*, be relevant for DNA origami sensing systems that incorporate glass nanocapillary pores with a sensing length of a few hundred nanometers (*cf.* Sec. A in the Appendix for an estimating calculation) and an analyte with a similar or smaller length<sup>36</sup>.

In this study, we present results for a finite pore model in terms of a mean-field level description of the two-reservoir setup in which a DNA molecule is fixed in the center of the pore. Our results show that the ionic current through the pore significantly depends on the molecule length for a range of

electrolyte concentrations that typically contain the concentration of zero modulation. Furthermore, we present an interesting effect of a large current modulation when only one of the DNA ends is present in the pore. These effects are expected to be much more noticeable for pores with a large sensing length and cannot be resolved in typical DNA sensing setups with solid-state nanopores due to the high demands on the ionic current sampling rate on the order of hundreds of MHz.

Although we are not explicitly modeling a system of DNA origamis, the physical mechanism, *i. e.* the ion cloud polarization, leading to the observed reduction in the ionic current is transferable to such systems. Future modeling approaches in this direction based on the work presented here might also explain the non-monotonic behavior of the cross-over salt concentration as a function of the length of the origami molecule as observed by Wang, Ermann, and Keyser<sup>36</sup>.

## II. THE DNA-NANOPORE MODEL

The model under study incorporates two electrolyte reservoirs with a monovalent electrolyte solution of varying concentration that are connected by a cylindrical nanopore. The DNA is modeled as a cylindrical object with rounded ends fixed at the center of the pore. The DNA ends are modeled as hemispherical caps of the same diameter as the DNA. We mainly follow the modeling approach as described in Ref. 28. However, while Ref. 28 neglects any finite size effects of the pore and the DNA molecule, the model in this work explicitly takes these effects into account. The sketch in Fig. 1 shows the whole simulation domain with the two electrolyte reservoirs, the connecting nanopore and the DNA in the center of the pore. The diameter of the pore is 10 nm while the investigated pore length is 40 nm. The length of the DNA is varied in the range from 0.4 to 1.6 pore lengths (*i. e.* 16 nm to 64 nm) in order to also investigate the conductivity for systems where the DNA is significantly shorter or larger than the nanopore. The overall system length has been set to 10 times the pore length.

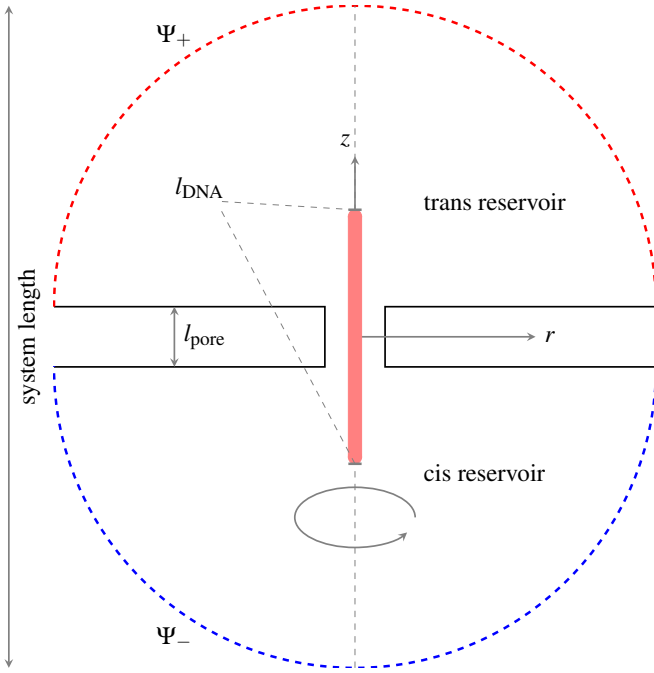


FIG. 1. A sketch of the mean-field model of a nanopore with finite length. The system is axisymmetric and can therefore be treated in two dimensions. The hemispheric areas at the top and the bottom correspond to the cis and trans electrolyte reservoirs.

The mean-field model employed in this work is based on solving the electrokinetic equations (Poisson for electrostatics, Nernst-Planck for ion transport, and Stokes for hydrodynamics of the solvent) for a charged cylinder representing the dsDNA in an uncharged cylinder representing the nanopore following the approach in Ref. 28. The Nernst-Planck equation is modified to incorporate the friction between ions and the dsDNA molecule that has previously been found to be crucial for coarsened dsDNA models in order to reproduce experimental and all-atom simulation data on current modulation in nanopores<sup>22,27</sup>.

The diffusion-advection equation for the fluxes of the ionic species  $\mathbf{j}_{\pm}$  in the system reads:

$$\mathbf{j}_{\pm} = [-D\nabla + \mathbf{u} + \mu_{\pm}\mathbf{F}_{\pm}]c_{\pm}, \quad (1)$$

where  $D_{\pm}$  is the diffusion constant,  $\mathbf{u}$  is the fluid velocity,  $\mu_{\pm} = \mu = \frac{D}{k_B T} = 4.8286 \times 10^{11} \text{ s kg}^{-1}$  is the ion mobility,  $\mathbf{F}_{\pm}$  contains any external forces, and  $c_{\pm}$  the ion density. The external forces are comprised of the electrostatic forces and the frictional forces:

$$\mathbf{F}_{\pm} = e z_{\pm} \mathbf{E} - \alpha \omega \left( 0, 0, \frac{j_{\pm}^z}{c_{\pm}} \right)^{\top}. \quad (2)$$

Due to the velocity-dependent frictional force, this results in an algebraic equation for the fluxes along the pore ( $z$ -

component):

$$j_{\pm}^z(r, z) = \left[ -D \frac{\partial}{\partial z} + u^z(r, z) + \mu \left( e z_{\pm} E^z(r, z) - \alpha \omega(r, z) \frac{j_{\pm}^z(r, z)}{c_{\pm}(r, z)} \right) \right] c_{\pm}(r, z), \quad (3)$$

where  $e$  is the elementary charge,  $z_{\pm}$  the valency of the ions,  $E^z$  the electric field strength along the symmetry axis,  $\alpha = 15 \times 10^{-12} \text{ kg s}^{-1}$  a numerical constant (controlling the amount of frictional force) and  $\omega$  is a position-dependent weight function for the frictional force (adopted from Ref. 28):

$$\omega(r, z) = \begin{cases} \left( 1 - \frac{r}{r_{\text{cut}}} \right)^2 & \text{if } r < r_{\text{cut}} \text{ and } |z| < \frac{l_{\text{DNA}}}{2}, \\ 0 & \text{else,} \end{cases} \quad (4)$$

where  $r_{\text{cut}} = 1.4 \text{ nm}$  is the cut-off distance for the friction. We assume a temperature of 300 K throughout all simulations.

The advective motion of ions is taken into account by means of Stokes' equations with incompressibility condition:

$$\eta \nabla^2 \mathbf{u} - \nabla p + \mathbf{f} = 0, \quad (5)$$

$$\nabla \cdot \mathbf{u} = 0, \quad (6)$$

where  $\eta$  is the dynamic viscosity,  $\mathbf{u}$  the fluid velocity,  $p$  the pressure, and  $\mathbf{f} = \sum_{i \in \{+, -\}} c_i \mathbf{F}_i$  (cf. Eq. (2)) is the force density that the ions impose on the fluid. A no-slip boundary condition  $\mathbf{u} = 0$  is applied on both the pore and DNA surface. Hydrodynamic momentum exchange over the reservoir boundaries (dashed lines in Fig. 1) is prevented by applying a vanishing normal stress condition for the fluid flow.

Electrostatic interactions between ions are considered by solving the Poisson equation

$$\nabla^2 \Psi = - \frac{\sum_{i \in \{+, -\}} e z_i c_i}{\epsilon_0 \epsilon_r}, \quad (7)$$

where  $\Psi$  is the electrostatic potential with vacuum permittivity  $\epsilon_0$  and the relative permittivity of water  $\epsilon_r = 78.54$ <sup>37</sup>. On the DNA boundary, we set the surface charge density  $\sigma = -0.136 \text{ C/m}^2$ . For the pore surface a zero-charge condition  $\mathbf{n} \cdot \nabla \Psi = 0$  is applied, where  $\mathbf{n}$  denotes the unit vector normal to the boundary. For the lower and upper boundaries (drawn with blue and red dashed lines in Fig. 1, respectively) we set the electrostatic potentials  $\Psi_- = 0$  and  $\Psi_+ = l_{\text{pore}} E_{\text{ext}}^z$  with  $l_{\text{pore}}$  being the length of the pore and  $E_{\text{ext}}^z = 1 \times 10^6 \text{ V m}^{-1}$  being the approximate value for the electric field in comparable experimental setups<sup>36</sup>. By choosing the electrostatic potential difference depending on the pore length and thereby keeping the electric field in the pore approximately constant we are able to directly compare results from different pores. The friction between ions and dsDNA results in a coupling between electrostatic and advective forces on the ions. The model's inherent axisymmetry reduces the problem domain to two dimensions. We solved the electrokinetic equations with the finite-element method using the commercial software package COMSOL Multiphysics<sup>®</sup> version 5.6. (cf. Sec. D in the Appendix for information about the used FEM mesh).

### III. RESULTS

The central physical quantity of interest is the ionic current through the DNA nanopore system. In analogy to previous experimental and theoretical studies<sup>9,28,35,36</sup>, we define the following pore length independent current modulation:

$$I_{\text{mod}} := \frac{I_{\text{filled}} - I_{\text{empty}}}{I_{\text{empty}}}, \quad (8)$$

where  $I_{\text{filled}}$  is the ionic current through the pore if a test molecule is present in the pore and  $I_{\text{empty}}$  is the empty pore current. In Fig. 2, the ionic current modulation is shown as a function of the DNA length for different electrolyte bulk concentrations. There is a significant drop in the modulation for shorter DNA molecules if the molecule length falls below the pore length.

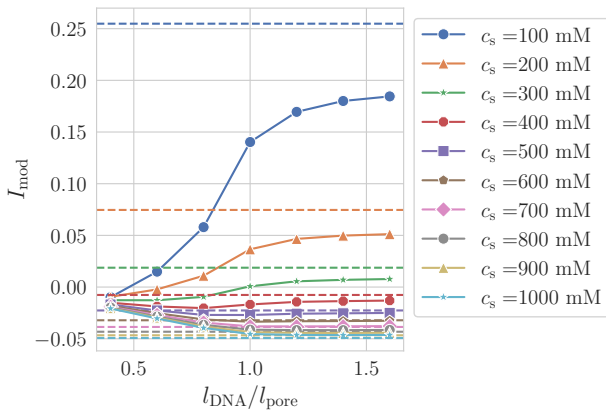


FIG. 2. The ionic current modulation as a function of the DNA molecule's length for different salt concentrations. The length of the nanopore is 40 nm. The dashed lines show the current modulation for an infinite pore (taken from results for the model as presented in Ref. 28).

Comparing the current modulation to data from the infinite pore model of Ref. 28 (*cf.* Fig. 3), the curves for the finite pore seem to converge towards the infinite pore reference for increasing ratios of  $l_{\text{DNA}}/l_{\text{pore}}$ . The differences in the modulation are larger for shorter molecules and smaller salt concentrations. Consistent with results from all-atom simulations of an infinite pore system as presented in Ref. 22, the ionic current through the pore is dominated by the direct contribution caused by the applied electric field (*cf.* Eq. (9)). As can be seen in Fig. 4a, the advective current fraction due to electroosmotic flow along the DNA is at most in the order of 5–6 percent. Notably, the ionic current's dependency on the DNA length has its maximum for the lowest salt concentration, *i. e.* where the negatively-charged surface is screened least. This is in line with the salt-dependent ionic current modulation in experimental systems<sup>9,36</sup> and simulation studies<sup>22,28,35</sup> of similar systems in which the current modulation diverges in the limit of zero bulk electrolyte concentrations.

Because of the much larger influence of the direct current on the total current modulation, we focus further analysis on

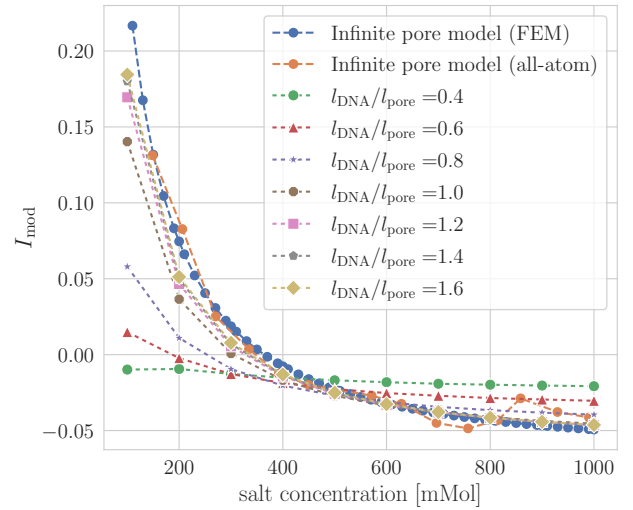


FIG. 3. The ionic current modulation as a function of salt concentration different DNA molecule lengths. The data is also compared to results from two infinite pore models on the mean-field level<sup>28</sup> and the atomistic level of detail<sup>22</sup>.

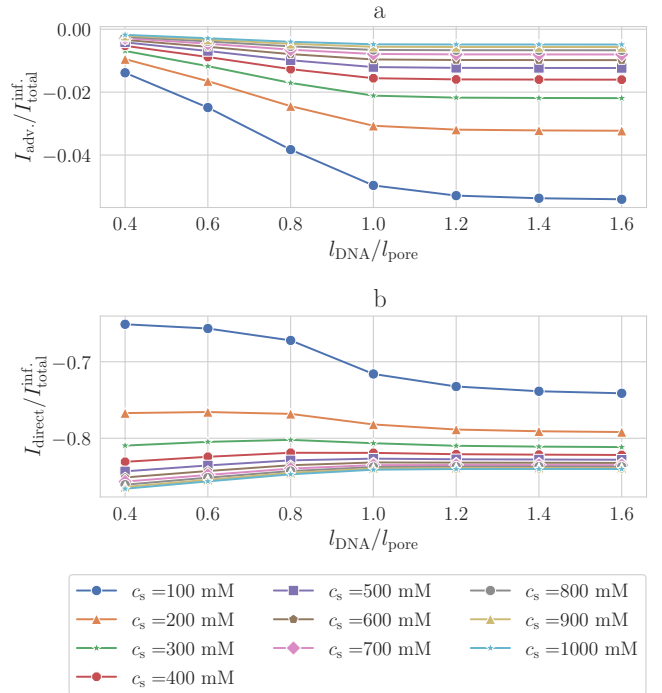


FIG. 4. The advective (a) and direct (b) contributions to the ionic current as a function of the DNA length.

the electric field and the amount of charge in the pore since these quantities actually define the direct current density (neglecting constants):

$$j_{\text{direct}}^z(r, z) = \frac{\mu e^2 E_z(r, z) [c_+(r, z) + c_-(r, z)]}{\alpha \mu \omega(r, z) + 1}, \quad (9)$$

where we reused the notation of Eq. 3.

In order to investigate the electric field's dependency on the DNA length we radially averaged the  $z$ -component of the field at the center of the pore ( $z = 0$  and  $r \in [r_{\text{DNA}}, r_{\text{pore}}]$ ). Along this horizontal line, the electric field vanishes for symmetry reasons if no external field acts on the mobile charges of the system. However, as can be seen in Fig. 5 if an external field is applied we observe a significant modulation of the electric field along the pore as a function of the DNA length for small electrolyte concentrations. In the most intuitive picture on the level of an equivalent circuit model for the DNA nanopore system the DNA acts as an increased resistance in the pore and the total resistance of the DNA increases with its length. Thus, a larger portion of the potential drops along the DNA which increases the electric field in the pore. However, as Fig. 2 shows, the DNA actually enhances the current in the pore (for bulk electrolyte concentrations up to around  $400 \text{ mmol l}^{-1}$ ). Therefore, this simplified picture can not explain our observation of an increased electric field.

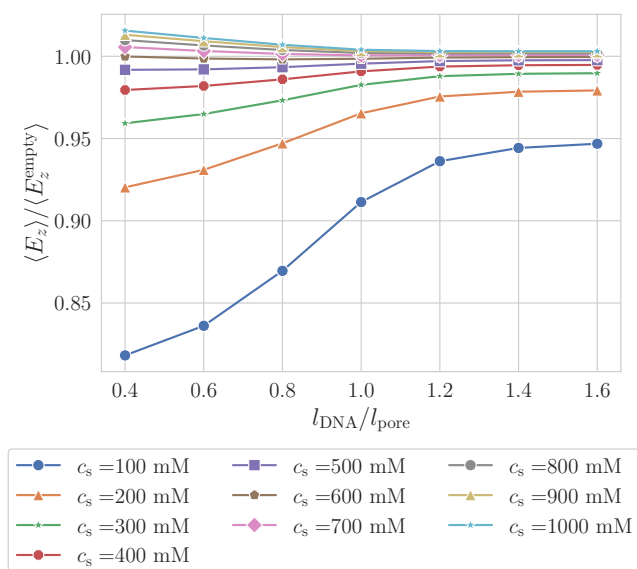


FIG. 5. The average  $z$ -component of the electric field in the center of the pore as a function of the DNA length normalized by the average  $z$ -component of the electric field in the center of an empty pore.

The external electric field induces an electric dipole field caused by the polarized counter-ion cloud around the negatively charged DNA that weakens the externally applied field in the pore. Fig. 6 shows the dependency of this dipole moment on the DNA length. Here, again we see a significant dependency on the DNA length for low salt concentrations. In addition, the induced dipole moment decreases with the salt concentration. Intuitively one might think that a larger dipole moment would lead to a larger opposing field and therefore a weaker total field in the pore center. The dipole electric field in the pore center, however, also depends on the locations of the charges.

In the following, we want to develop a simple model to get a better understanding of what the induced dipole moment's

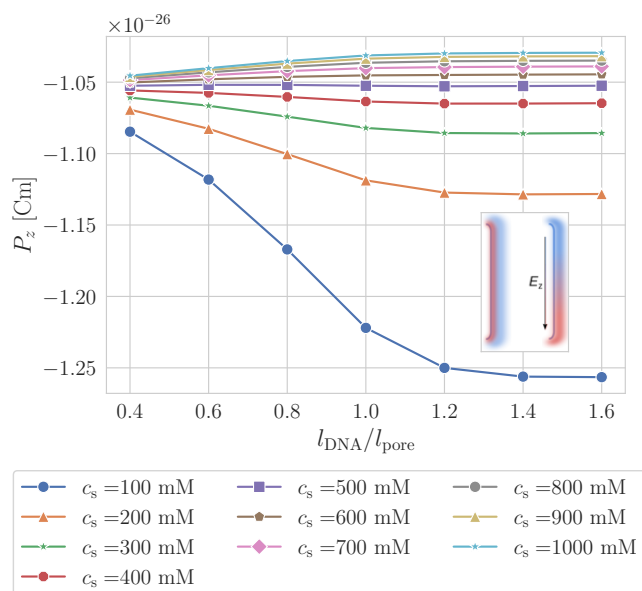


FIG. 6. The  $z$ -component of the total electric dipole of the whole simulation domain. The inset image shows a sketch of the ion cloud around the charged surface of the DNA: the external field induces an asymmetry in the mobile ion distribution.

data actually means for the electric field in the pore. In this model we assume that all electrostatic effects of the mobile ions and the negatively charged DNA are included in the resulting electric dipole field. We therefore calculate the electric field of two charges that are located at the two ends of the DNA on the symmetry axis of the system at  $(\pm 0.5l_{\text{DNA}})$ . This results in an electric field in the center of the pore (*cf.* Sec. C in the Appendix):

$$E_z^{\text{dipole}}(r, z = 0) = \frac{2|P_z|}{\pi\epsilon_0\epsilon_r(l_{\text{DNA}}^2 + 4r^2)^{\frac{3}{2}}}, \quad (10)$$

where  $P_z$  is the induced dipole moment,  $\epsilon_0$  is the vacuum permittivity and  $\epsilon_r$  is the permittivity of water. The resulting electric field radially averaged over the pore at  $z = 0$  decreases with increasing DNA length (*cf.* Fig. 12 in the Appendix) which explains the observation of an increasing total electric field in the pore center: the decreasing electric field strength of the induced dipole has less influence on the total electric field for longer DNA molecules. In addition, there is a reduced influence of the electric field on the DNA length for increasing electrolyte concentrations. From  $c_s \approx 700 \text{ mmol l}^{-1}$  on the DNA charge seems to be completely screened. For these high salt concentrations the DNA can be seen as an additional resistor, therefore causing a higher portion of the electrostatic potential to drop along the DNA which is equivalent to a larger electric field strength.

The second contributing factor to the direct current is the total charge in the pore. Therefore, we analyze the DNA length's influence on the ion density in the pore. In the pore, the presence of the negatively charged DNA repels the cations and attracts the counter-ions. In addition, this effect is

enhanced for longer DNA molecules (*cf.* Sec. B in the Appendix). The total ion density in the pore, however, is enhanced (compared to the reservoir) and increases with the length of the DNA. Therefore, the repulsion of co-ions is overcompensated by the attraction of the counter-ions (*cf.* Fig. 7). This observation is in line with the overall observation of a larger ionic current through the pore for electrolyte concentrations of up to about  $400 \text{ mol l}^{-1}$ .

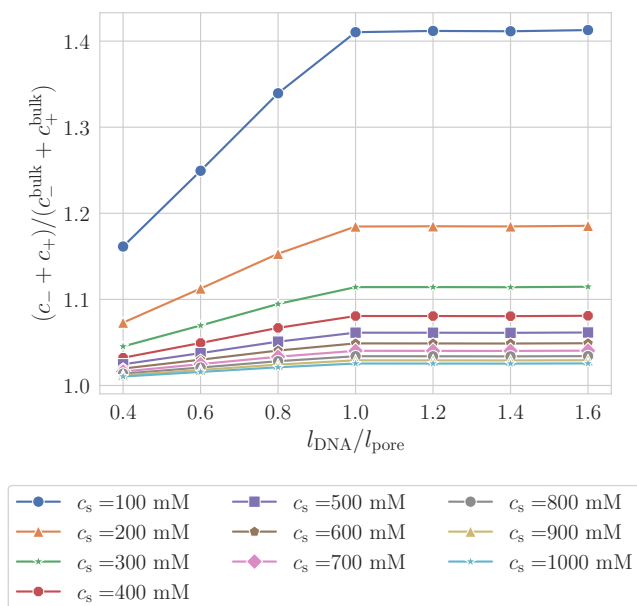


FIG. 7. The averaged total ion density in the pore normalized with the respective bulk values as a function of the DNA length.

Fig. 8 shows an interesting effect of an enhanced ionic current modulation that we observe in the two phases of the translocation process in which only one end of the DNA is located in the pore. Notably, this modulation is about a factor of four larger compared to the situation where neither of the DNA ends is in the pore. This high modulation is only observed for a relatively short part of the translocation of about 20 nm in our pore geometry and therefore the sampling frequency of experimental setups would need to be sufficiently large to capture such effects. The translocation speed of a DNA through a solid state nanopore is about  $1 \times 10^6 \text{ bps}^{-1}$  to  $1 \times 10^8 \text{ bps}^{-1}$ , *i. e.*  $0.34 \text{ mm s}^{-1}$  to  $34.0 \text{ mm s}^{-1}$  <sup>38,39</sup>. That means that the time interval that has to be resolved in the experiment is about  $\Delta t \approx 0.588 \mu\text{s}$  to  $5.88 \mu\text{s}$  which translates to a sampling rate of about 1.7 MHz to 17 MHz. However, since the high modulation is present as long as only one of the analyte ends is in the sensing region, it might be possible to resolve the modulation for pores with a longer sensing length, *e. g.* in glass nanopipillaries. Still, we are not aware of experimental observations of similar effects.

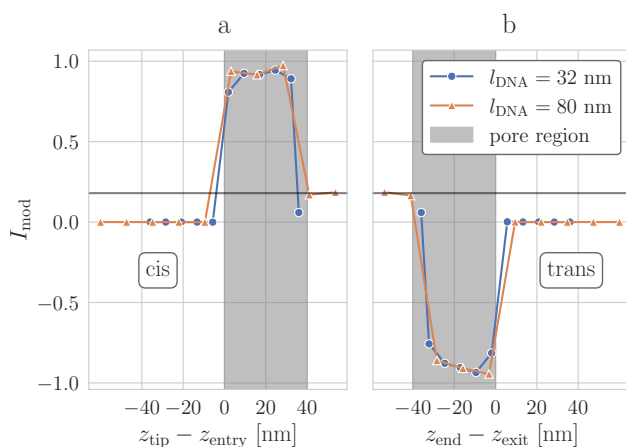


FIG. 8. The ionic current modulation (*cf.* Eq. (8)) as a function of the distance between the DNA tip and the pore entry (a) and as a function of the distance between the DNA end and the pore exit (b) for two different DNA lengths. The horizontal line shows the approximate modulation when both DNA ends are outside of the pore region.

#### IV. CONCLUSION

We have shown that the current modulation of analytes in nanopore sensing setups significantly depends on the length of the translocating charged object if the length of the object is shorter than the sensing length of the pore for electrolyte concentrations up to about  $400 \text{ mmol l}^{-1}$ . Our model in this work extends a previously studied mean-field model<sup>28</sup> for an infinite dsDNA molecule in an infinite pore to a model that includes a finite pore and the cis- and trans-reservoirs of the Coulter-type sensing setup. Our data shows that the ionic current increases with the length of the DNA and converges to values of infinite pore models as presented in Refs. 22, 28, 35, and 40. Furthermore, we investigated the underlying electrostatic effects, namely the length-dependent opposing electric field that results from the polarized ion cloud around the DNA. This dipole field's component parallel to the pore gets smaller for an increasing DNA length which leads to an overall increasing electric field in the pore. Such effects are not present in our infinite pore models for DNA origamis as presented in Ref. 35 which might explain the deviation between the simulation data of these models and experimental results of Wang, Ermann, and Keyser<sup>36</sup>.

In addition, our simulations revealed an interesting effect, namely the appearance of an enhanced ionic current modulation upon just entering or just leaving the nanopore interior that can be ascribed to the local electric field of the charged molecule's tip either amplifying or weakening the externally applied electric field in the pore.

#### ACKNOWLEDGMENTS

We thank Florian Weik, Alexander Schlaich, Jonas Lands-gesell and Georg Rempfer for helpful and constructive dis-

cussions. The work is funded by the Deutsche Forschungsgemeinschaft (DFG, German Science Foundation) — Project Number 390740016 — EXC 2075 “SimTech”.

## DATA AVAILABILITY STATEMENT

The data that support the findings of this study are available from the corresponding author upon reasonable request.

## Appendix A: Effective Pore Length

In experimental studies of Wang, Ermann, and Keyser<sup>36</sup> a similar setup to the model presented in this manuscript has been utilized to investigate the current modulation of complex DNA structures. One of the more significant differences, however, is the pore geometry. The glass capillaries used in the experimental study have a diameter of about 10 nm at the tip but have a conical geometry with an opening angle of about 6°. It is known from experimental<sup>29</sup> as well as simulation studies<sup>28</sup> that a wider nanopore causes a larger magnitude of electroosmotic flow which leads to a larger contribution of the advective current to the overall ionic current. However, all-atom simulations in an infinite cylindrical pore setup<sup>22</sup> revealed that this contribution is negligible for infinite DNA nanopore systems. Nevertheless, even if this geometric effect might not be significant for the conductivity of the system, the absolute length of the nanopore might influence the importance of the finite size effects. To get an estimate for up to which length the conicity of the experimental pore affects the conductivity, we calculated the length-dependent pore resistance. For an infinitesimal pore segment of length  $dz$  the resistance of a conical pore with the cross-section area  $A(z)$  can be described as

$$dR = \rho \frac{dz}{A(z)}, \quad (\text{A1})$$

where  $\rho$  is the bulk electrolyte resistance and  $A(z) = \pi r(z)^2 = \pi(r_1 + z \tan \alpha)^2$  is the cross-section area of the pore at the position  $z$  measured from the tip of the pore. Here,  $\alpha$  denotes the opening angle of the conical pore geometry. Integrating Eq. A1 yields:

$$R(z) = \rho \int_0^z \frac{1}{A(\tilde{z})} d\tilde{z} = \frac{\rho}{\pi} \frac{z}{(r_1(z + \frac{r_1}{\tan \alpha})) \tan \alpha} \quad (\text{A2})$$

In Fig. 9, Eq. A2 is shown for a pore length up to 1  $\mu\text{m}$ . The value of the bulk resistance  $\rho$  is arbitrarily set to unity. In the limit of an infinitely long conical pore Eq. (A2) converges to a resistance of  $R_\infty = \frac{\rho}{\pi \tan(\alpha) r_1}$ . However, as shown in Fig. 9, the largest contribution to the resistance (95 % at about 900 nm) suggests an effective length of the pore on the order of several hundred nanometers. Although this model only takes into account the resistance based on the geometry of the pore, the result is in line with simulation studies in Ref. 15 in which the decay of the electric field in the pore was used to estimate the sensing length.

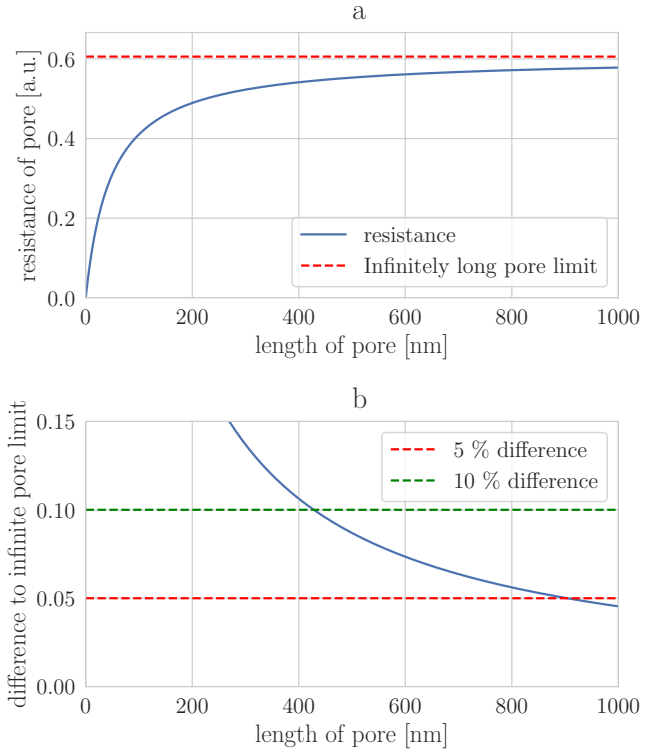


FIG. 9. Length-dependent pore resistance for a conical pore and the respective resistance in the infinite pore limit (a). The difference between the resistance of the conical pore with a given length and the infinite pore limit (b). The crossing of the 5 % line and the resistance curve is at about 900 nm.

The DNA structures studied by Wang *et al.* in Ref. 36 are between approximately 150 nm and 600 nm and are therefore shorter than the estimated effective pore length. This clearly sets those DNA nanopore systems apart from many other experimentally investigated setups in which the DNA is orders of magnitude longer than the pore.

## Appendix B: Ion Density in the Pore

We analyzed the density of the two ion species in the pore. The co-ions of the dsDNA are repelled from the pore and the density is well below the bulk value for all investigated DNA lengths and salt concentrations. The cation density, however, is enhanced in the pore and increases with the length of the DNA (*cf.* Fig. 10).

## Appendix C: Electric Dipole Field Model

This model assumes that the  $z$ -component of the total dipole moment DNA nanopore system is created by a single pair of charges at the two ends of the DNA on the symmetry axis. This assumption is based on the observation that the charge density is asymmetric along the DNA as shown in Fig. 11.

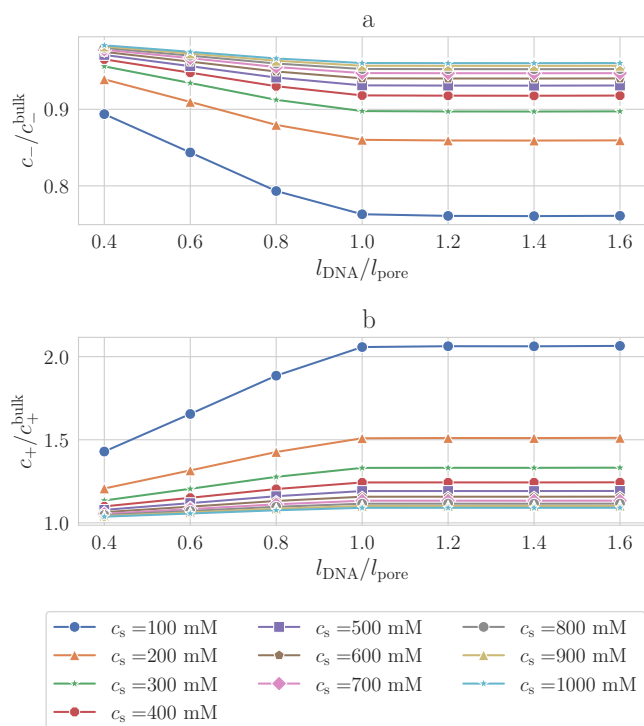


FIG. 10. The average anion (a) and cation density (b) in the pore normalized with the respective bulk values as a function of the DNA length.

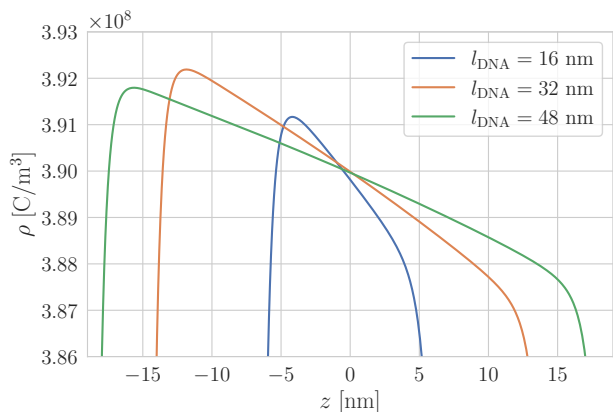


FIG. 11. The charge density along the  $z$ -axis at  $r = r_{\text{DNA}}$  for three different DNA lengths. The ion cloud at the vicinity of the DNA is asymmetric due to the externally applied electric field.

Thus, the electrostatic potential of these two charges ( $+q$  at

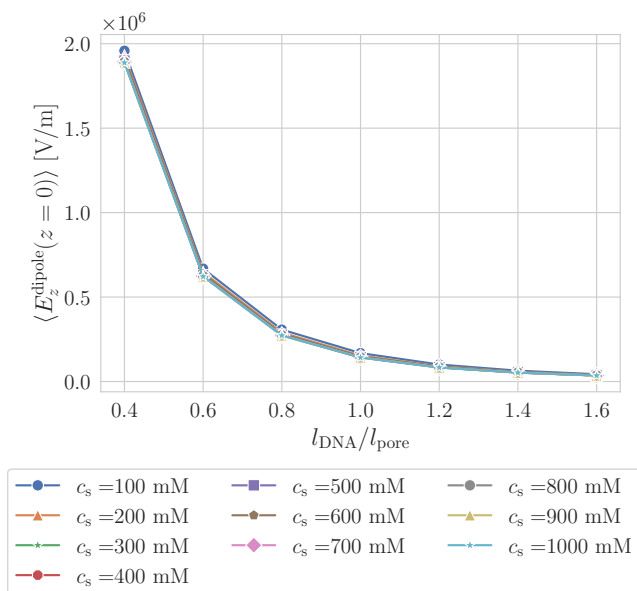


FIG. 12. The average  $z$ -component of the electric field caused by a single

$z = -0.5 l_{\text{DNA}}$  and  $-q$  at  $z = 0.5 l_{\text{DNA}}$ ) reads:

$$\Phi(r, z) = \frac{|q|}{4\pi\epsilon_0\epsilon_r} \left[ \left( r^2 + \left( z + \frac{l_{\text{DNA}}}{2} \right)^2 \right)^{-\frac{1}{2}} - \left( r^2 + \left( z - \frac{l_{\text{DNA}}}{2} \right)^2 \right)^{-\frac{1}{2}} \right]. \quad (\text{C1})$$

From the electrostatic potential, the  $z$ -component of the electric field at  $z = 0$  can be calculated by taking the negative gradient of the potential:

$$E_z^{\text{dipole}}(r, z = 0) = (-\nabla\Phi(r, z))_{z, z=0} = \frac{2|q|l_{\text{DNA}}}{\pi\epsilon_0\epsilon_r(l_{\text{DNA}}^2 + 4r^2)^{\frac{3}{2}}}. \quad (\text{C2})$$

We now insert the assumption that the system's total dipole moment is only caused by the two charges, *i. e.*  $|q| = \frac{|P_z|}{l_{\text{DNA}}}$

$$E_z^{\text{dipole}}(r, z = 0) = \frac{2|P_z|}{\pi\epsilon_0\epsilon_r(l_{\text{DNA}}^2 + 4r^2)^{\frac{3}{2}}}. \quad (\text{C3})$$

#### Appendix D: FEM Mesh

The rotational symmetry of the investigated three-dimensional system setup allows for its treatment using a quasi-two-dimensional axisymmetric simulation domain. The FEM mesh for this domain was adapted (*cf.* Fig. 13) in order to properly resolve the Debye layer near the negatively charged DNA. Using quadrilateral elements close to the DNA

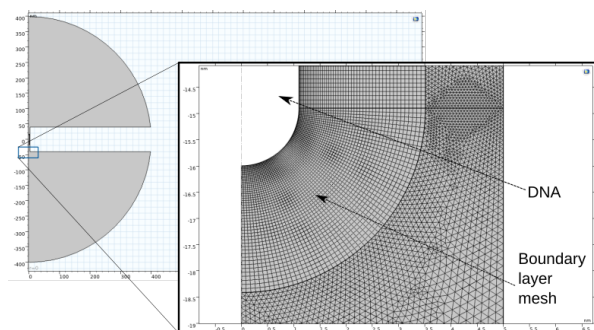


FIG. 13. Example of the customized mesh used for the FEM simulations. The area around the electrically charged DNA surface is resolved with quadrilateral elements to properly capture the behavior in the Debye layer. The rest of the simulation domain consists of triangular mesh elements.

surface, the geometry of the mesh more closely follows the expected symmetry of the solution for the Poisson equation for electrostatics which defines the smallest length scale in the investigated DNA nanopore system.

- <sup>1</sup>B. Venkatesan and R. Bashir, *Nature Nanotechnology* **6**, 615 (2011).
- <sup>2</sup>D. Rotem, L. Jayasinghe, M. Salichou, and H. Bayley, *Journal of the American Chemical Society* **134**, 2781 (2012).
- <sup>3</sup>K. Lewandowski, Y. Xu, S. T. Pullan, S. F. Lumley, D. Foster, N. Sanderson, A. Vaughan, M. Morgan, N. Bright, J. Kavanagh, R. Vipond, M. Carroll, A. C. Marriott, K. E. Gooch, M. Andersson, K. Jeffery, T. E. A. Peto, D. W. Crook, A. S. Walker, and P. C. Matthews, *Journal of Clinical Microbiology* **58**, e00963 (2019).
- <sup>4</sup>M. Taniguchi, S. Minami, C. Ono, R. Hamajima, A. Morimura, S. Hamaguchi, Y. Akeda, Y. Kanai, T. Kobayashi, W. Kamitani, *et al.*, *Nature Communications* **12**, 1 (2021).
- <sup>5</sup>S. Howorka, S. Cheley, and H. Bayley, *Nature Biotechnology* **19**, 636 (2001).
- <sup>6</sup>D. Fologea, M. Gershow, B. Ledden, D. S. McNabb, J. A. Golovchenko, and J. Li, *Nano Letters* **5**, 1905 (2005).
- <sup>7</sup>A. J. Storm, J. H. Chen, H. W. Zandbergen, and C. Dekker, *Physical Review E* **71**, 051903 (2005).
- <sup>8</sup>A. J. Storm, C. Storm, J. Chen, H. Zandbergen, J.-F. Joanny, and C. Dekker, *Nano Letters* **5**, 1193 (2005).
- <sup>9</sup>R. M. M. Smeets, U. F. Keyser, D. Krapf, M.-Y. Wu, N. H. Dekker, and C. Dekker, *Nano Letters* **6**, 89 (2006).
- <sup>10</sup>U. Keyser, J. van der Does, C. Dekker, and N. Dekker, *Review of Scientific Instruments* **77**, 105105 (2006).
- <sup>11</sup>U. Keyser, B. Koeleman, S. van Dorp, D. Krapf, R. Smeets, S. Lemay, N. Dekker, and C. Dekker, *Nature Physics* **2**, 473 (2006).
- <sup>12</sup>J. Clarke, H.-C. Wu, L. Jayasinghe, A. Patel, S. Reid, and H. Bayley, *Nature Nanotechnology* **4**, 265 (2009).
- <sup>13</sup>L. J. Steinbock, A. Lucas, O. Otto, and U. F. Keyser, *Electrophoresis* **33**, 3480 (2012).
- <sup>14</sup>L. J. Steinbock and U. F. Keyser, “Analyzing single DNA molecules by nanopore translocation,” in *Nanopore-Based Technology*, edited by M. E. Gracheva (Springer, 2012) Chap. 7, pp. 135–145.
- <sup>15</sup>N. A. Bell, M. Muthukumar, and U. F. Keyser, *Physical Review E* **93**, 022401 (2016).
- <sup>16</sup>B. Miles, A. Ivanov, K. Wilson, F. Dogan, D. Japrun, and J. Edel, *Chemical Society Reviews* **42**, 15 (2013).
- <sup>17</sup>B. Luan and A. Aksimentiev, *Physical Review E* **78**, 021912 (2008).
- <sup>18</sup>U. F. Keyser, S. van Dorp, and S. G. Lemay, *Chemical Society Reviews* **39**, 939 (2010).
- <sup>19</sup>S. Getfert, T. Töws, and P. Reimann, *Physical Review E* **87**, 062710 (2013).
- <sup>20</sup>W.-J. Lan, D. A. Holden, B. Zhang, and H. S. White, *Analytical Chemistry* **83**, 3840 (2011).
- <sup>21</sup>N. Laohakunakorn, S. Ghosal, O. Otto, K. Misiunas, and U. F. Keyser, *Nano Letters* **13**, 2798 (2013).
- <sup>22</sup>S. Kesselheim, W. Müller, and C. Holm, *Physical Review Letters* **112**, 018101 (2014).
- <sup>23</sup>L.-H. Yeh, M. Zhang, S. Qian, and J.-P. Hsu, *Nanoscale* **4**, 2685 (2012).
- <sup>24</sup>G. Rempfer, G. B. Davies, C. Holm, and J. de Graaf, *The Journal of Chemical Physics* **145**, 044901 (2016).
- <sup>25</sup>G. Rempfer, S. Ehrhardt, N. Laohakunakorn, G. B. Davies, U. F. Keyser, C. Holm, and J. de Graaf, *Langmuir* **32**, 8525 (2016).
- <sup>26</sup>G. Rempfer, S. Ehrhardt, C. Holm, and J. de Graaf, *Macromolecular Theory and Simulations* **26**, 1600051 (2017).
- <sup>27</sup>F. Weik, S. Kesselheim, and C. Holm, *The Journal of Chemical Physics* **145**, 194106 (2016).
- <sup>28</sup>F. Weik, K. Szuttor, J. Landsgesell, and C. Holm, *European Physical Journal Special Topics* **227**, 1639 (2019).
- <sup>29</sup>S. van Dorp, U. F. Keyser, N. H. Dekker, C. Dekker, and S. G. Lemay, *Nature Physics* **5**, 347 (2009).
- <sup>30</sup>J. H. Chaudhry, J. Comer, A. Aksimentiev, and L. N. Olson, *Communications in computational physics* **15**, 93 (2014).
- <sup>31</sup>A. Aksimentiev, *Nanoscale* **2**, 468 (2010).
- <sup>32</sup>L. Luo, S. R. German, W.-J. Lan, D. A. Holden, T. L. Mega, and H. S. White, *Annual Review of Analytical Chemistry* **7**, 513 (2014).
- <sup>33</sup>M. Fyta, *Journal of Physics: Condensed Matter* **27**, 273101 (2015).
- <sup>34</sup>S. Ghosal, J. D. Sherwood, and H.-C. Chang, *Biomicrofluidics* **13**, 011301 (2019).
- <sup>35</sup>K. Szuttor, F. Weik, J.-N. Grad, and C. Holm, *The Journal of Chemical Physics* **154**, 054901 (2021), arXiv:2011.12908 [cond-mat.soft].
- <sup>36</sup>V. Wang, N. Ermann, and U. F. Keyser, *Nano Letters* **19**, 5661 (2019).
- <sup>37</sup>A. V. Wolf, M. G. Brown, and P. G. Prentiss, in *CRC Handbook of Chemistry and Physics*, edited by R. C. Weast (CRC Press, Boca Raton, 1986) 67th ed., pp. D–253.
- <sup>38</sup>C. Plesa, N. Van Loo, P. Ketterer, H. Dietz, and C. Dekker, *Nano Letters* **15**, 732 (2015).
- <sup>39</sup>S. J. Heerema, L. Vicarelli, S. Pud, R. N. Schouten, H. W. Zandbergen, and C. Dekker, *ACS Nano* **12**, 2623 (2018).
- <sup>40</sup>T. Rau, F. Weik, and C. Holm, *Soft Matter* **13**, 3918 (2017).